PAPER • OPEN ACCESS

Experimental validation of inventory simulations on molybdenum and its isotopes for fusion applications

OPEN ACCESS
IOP Publishing | International Atomic Energy Agency
Nuclear Fusion
Nucl. Fusion **60** (2020) 106022 (18pp)
https://doi.org/10.1088/1741-4326/aba99c

Experimental validation of inventory simulations on molybdenum and its isotopes for fusion applications

M.R. Gilbert, L.W. Packer and T. Stainer

Culham Centre for Fusion Energy, UKAEA, Culham Science Centre, Abingdon, OX14 3DB, United Kingdom of Great Britain and Northern Ireland

E-mail: mark.gilbert@ukaea.uk

Received 6 May 2020, revised 21 July 2020
Accepted for publication 27 July 2020
Published 9 September 2020

Abstract

Molybdenum is a potential material for future nuclear fusion experiments and power plants. It has good thermo-mechanical properties and can be readily fabricated, making it attractive as an alternative material to tungsten (the current leading candidate) for high neutron flux and high thermal load regions of fusion devices. Unfortunately, exposure to fusion neutrons is predicted to cause significant radioactivity in elemental Mo for decades and centuries after exposure, which would be a problem during maintenance and decommissioning operations. Simulation predictions indicate that Mo activation could be reduced by isotopic adjustment (biasing). If these predictions are proven and validated, and if isotopic adjustment is technically and economically feasible, then Mo could be used in future demonstration and commercial reactors without significantly increasing the amount of long-term, higher-level radioactive waste.

Transmutation (inventory) simulations used to predict activation rely on nuclear reaction data. The quality of these data impact on the confidence and uncertainty associated with predictions. Recently, UKAEA has developed benchmarks to test and validate the FISPACT-II inventory code and the input nuclear data libraries. Verification of molybdenum inventory simulations is performed against experimental decay-heat measurements from JAEA's fusion neutron source (FNS) facility and using new data acquired from γ-spectroscopy measurements of Mo irradiated in the ASP 14 MeV facility in the UK.

Results demonstrate that FISPACT-II predictions (with TENDL-2019 nuclear data) for Mo are accurate on the short-timescales (minutes, hours of irradiation and minutes, days, weeks of cooling) of these laboratory experiments. However, these kinds of experiments are limited in their coverage of the important radionuclides for decay radiation from Mo on the years, decades and beyond timescales. Further experiments with fusion relevant conditions and timescales, potentially with alternative measurement techniques, are still needed.

Keywords: molybdenum, experimental validation, nuclear reactions, isotopic tailoring, inventory simulations, activation, radioactive waste

(Some figures may appear in colour only in the online journal)

1. Introduction: molybdenum as a fusion material

Molybdenum (Mo) is often proposed as an alternative material for the high neutron flux and high thermal load regions—the plasma-facing components (PFCs)—of nuclear fusion devices [1, 2]. While tungsten (W) is the main candidate [3, 4], difficulties with fabrication and issues

surrounding irradiation-induced embrittlement [3] lead to continued interest in alternatives, such as Mo. Mo exhibits similarly low sputtering yields [1] and equivalent thermal-mechanical properties to W (including similar thermal conductivity—around 140 and 170 W m^{-1} K^{-1} for Mo and W, respectively), while being potentially easier to fabricate (at room temperature) into fusion components [5, 6].

Aside from a straight replacement for W, Mo has also been used as an interlayer between W and base carbon tiles in JET as part of the ITER-like wall project [7, 8] because it has a good match with the thermal expansion coefficients of both W and C [6]. Mo and its alloys, particularly with rhenium (Re), also have a high strength and resistance to radiation swelling [9], and were once widely considered for the heat-sink of early divertor concepts for ITER (for example, see [9, 10]).

The PFC applications are more likely for Mo because less material would be required (compared to, for example, in the divertor heat-sink) and these are the regions where the use of pure W is currently envisaged. Unfortunately, these are also the regions where the neutron exposure is most severe, which is a problem for Mo because of its induced radioactivity (and γ dose [2]) under neutron irradiation. In particular, the activation is long-lived and high enough to present a barrier to the use of Mo (in its natural abundance isotopic form) in fusion due to the high-costs associated with disposal of fusion waste, the additional challenges in remote maintenance and recycling of highly activated components, and the public acceptability of long-lived radioactive waste.

1.1. Activation in EU-DEMO

For tungsten, the predicted radiological response is not too severe at long decay times (decades and beyond), although impurities introduced during the manufacture of industrial W, such as cobalt (Co) and potassium (K) at concentrations of around 0.001 weight % [11], could create a waste problem [12]. At short times (weeks, months, or even several years), W-based components of a fusion reactor (particularly the divertor) will require active cooling even after operation as significant residual decay heat will be generated by β-emitting radionuclides: ^{185}W ($T_{1/2}\approx$ 75 days) and ^{187}W (~ 24 hours) [11, 13].

Short-term activity is less of an issue for Mo; decay-heat and activity from Mo is predicted to be lower than in W after a typical fusion first wall exposure and around two-orders of magnitude lower after a year [14], which is confirmed by the calculations below (see figure 1). However, at longer timescales—decades and beyond—several problematic radionuclides are predicted to remain in naturally occurring Mo at levels sufficient to exceed regulatory limits for low-level waste (LLW) disposal. This makes it difficult to justify pure Mo for fusion applications where the goal is to avoid the generation of intermediate-level waste (ILW) requiring long-term deep geological disposal [12].

For example, if Mo were used instead of W for divertor PFCs (armour), or in the tritium-breeder-blanket first wall armour, of a recent conceptual design [15] for a

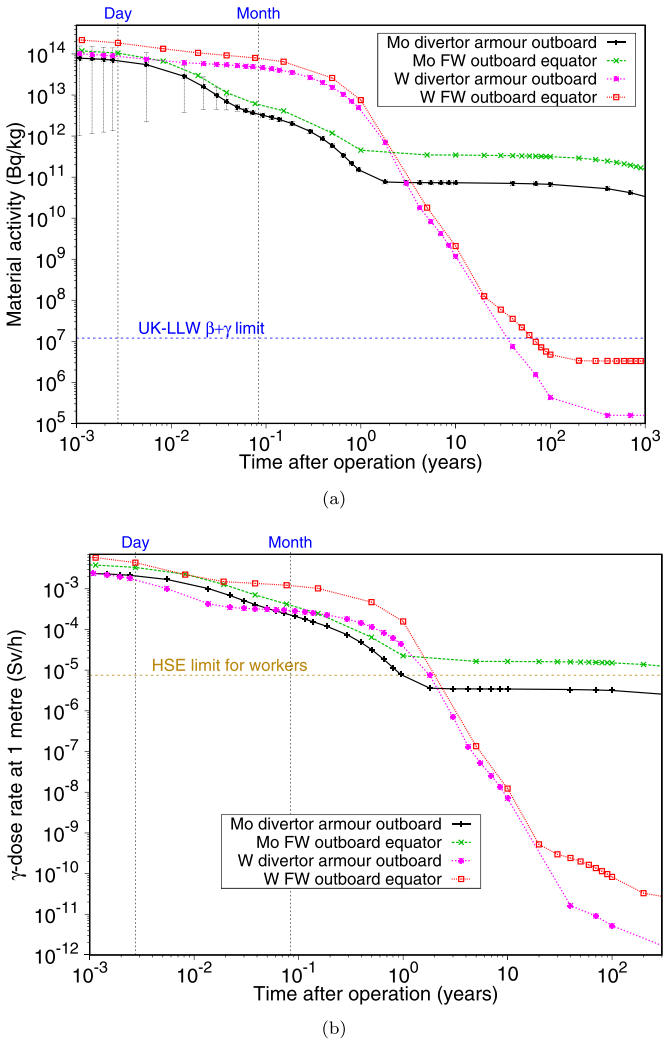

Figure 1. Simulation results for predicted post-operation activity of Mo and W (both with naturally occurring isotopic abundances) after typical fusion DEMO reactor exposures in the first wall (FW) of the blanket and in the armour tiles of the divertor. The post-operation activity in Bq/kg (*a*) and γ-dose-rate at 1 m in Sv/h (*b*) is shown as a function of time for natural Mo and W after typical component lifetimes (see main text for details).

European demonstration power plant (DEMO) then, after typical operating scenarios for that device, 'natural' Mo is predicted to exceed the 12 MBq kg^{-1} $\beta+\gamma$ emissions limit [16] for disposal in the UK's low-level, near-surface waste repositories for more than 1000 years. Here natural refers to Mo composed of its stable isotopes in their naturally occurring concentrations (^{92}Mo: 14.65%, ^{94}Mo: 9.19%, ^{95}Mo: 15.87%, ^{96}Mo: 16.67%, ^{97}Mo: 9.58%, ^{98}Mo: 24.29%, ^{100}Mo: 9.74%). This prediction is based on the results in figure 1(*a*), which shows the time-evolution in activation of irradiated Mo after the expected operational lifetime of divertor and blanket components in DEMO.

For this calculation, spectra of neutron fluxes as a function of energy were computed using Monte Carlo neutron-transport simulations (with MCNP [17]) for the 2015 DEMO baseline [15] design with a helium cooled tritium breeding

blanket made from a Pebble-Bed of beryllium and lithium-orthosilicate (abbreviated as HCPB; see [18] for details). Other tritium breeding concepts are also being considered within the EU-DEMO programme, including a water-cooled design with liquid lithium-lead (WCLL), but the neutron-spectra in the reactor-armour locations considered here are not significantly altered by the different blanket materials; WCLL versions of figure 1 are indistinguishable from those shown for HCPB.

Figure 2 shows the neutron flux spectra obtained from those calculations for the two reactor locations considered. Note that W was the armour material in these MCNP simulations; the spectra have the deep flux depressions associated with the giant neutron-capture resonances of W in the 1-100 eV energy range—a phenomenon known as self-shielding [19, 20].

It is always advisable to perform neutron-transport simulations with the correct material compositions in the geometry. However, for the purposes of the present work, where the focus is on a comparison of the radiological response of W and Mo, MCNP simulations have not been repeated with Mo as the armour material. For the thin armour layers where these spectra were recorded (2 and 5 mm thick for the armour of the blanket first wall and divertor, respectively), the main influence on the spectral shape and total flux comes from the bulk materials behind them: structural steels, coolant, and functional materials. Previous work (the activity analysis associated with [20]) demonstrated that, while subtle changes in the neutron spectrum caused by material variation can have significant impact on transmutation (composition change), the effect on activity is less profound and certainly not significant compared to the logarithmic variations shown in figure 1.

The two neutron spectra (one for the blanket and one for the divertor) were used in calculations performed with the FISPACT-II [21] inventory code; an inventory code predicts the time evolution of material compositions (from which the radiological response can be derived) using numerical solutions to the set of differential equations governing the rate-of-change of each nuclide in the system due to neutron irradiation and decay [21]. FISPACT-II was used with TENDL-2019 [22, 23] nuclear data to predict the material response to either ~5 years (for the divertor outboard target armour) or ~15 years (outboard equatorial blanket first wall armour) of pulsed operation; these are typical scenarios planned for DEMO, where the divertor is expected to be replaced every 5 years and the second phase of DEMO will use a single blanket for its entire 15-year campaign [11, 24]. Subsequently, FISPACT-II time-evolution was continued to track the post-operational decay activity and γ-dose-rate. Note that corrections for the capture-resonances, via probability tables, were included in the simulations for both Mo and W—see [20, 21] for details.

Figure 1(*a*) includes equivalent results for natural W in the two reactor regions considered and the difference compared to Mo is dramatic; W comfortably meets the UK $\beta+\gamma$-activity limit for LLW (shown in the plot as a horizontal line) in both the divertor and blanket armour cases on a reasonable 30-100 year timescale, while Mo exceeds it by several orders of magnitude even after 1000 years. Note that UK-LLW also has an α limit, but this is not relevant here as neither Mo or W produce α-emitting radionuclides under neutron irradiation.

Similarly, the γ-dose-rate from Mo is predicted to be many orders of magnitude higher than that from W from 10-years after the operational life of blanket and divertor components in DEMO. Figure 1(*b*) charts the time-evolution in γ-dose-rate, in units of Sv/h (Sieverts per hour), one metre from an idealised 1 g 'point source' of either Mo or W—this approximation of dose calculated by FISPACT-II is more conservative (lower) than the alternative, default, 'contact' dose approximation and is more relevant for radiation workers working in a nuclear environment and wearing protective clothing (a full γ-transport simulation is required for a more reliable prediction of γ-dose, see for example [26]). The UK's Health and Safety Executive (HSE) recommends, based on the UK's regulations for ionising radiation [27], a limit of 7.5 μSv/h (shown in the plot as a horizontal dashed line) for areas where workers will be exposed to ionising radiation [28]. While W, meets this limit within a year of post-operation cooling, the results show that Mo might pose a problem—the dose-rate predictions for Mo in the divertor falls below the HSE limit within a year but the dose-rate from Mo in the armour of the blanket remains above it for hundreds of years. Even the divertor result remains close to this limit (and thus still potentially presenting a handling and maintenance problem, especially if manufacturing impurities are taken into account [12]), while the dose-rate from W is predicted to fall below 1 nSv/h within 10 years.

1.2. Radioisotope contributions to Mo activity

Figure 3 illustrates the reasons behind the long-term high activity (and γ-dose) in Mo; it shows the time-evolution after operation in individual activity contributions from the different radionuclides (or radioisotopes) produced in Mo during the FISPACT-II simulation of 5 years in a divertor armour tile. The absolute activities (figure 3(*a*)) show that five radionuclides are each produced in sufficient quantities for their respective absolute activities to exceed the UK-LLW—four with half-lives of more than 500 years and a fifth, ^{93m}Nb, with a relatively short half-life, but whose concentration is in secular equilibrium with the long-lived ^{93}Mo that decays to it (see table 1), which is why their respective activities are identical. On the other hand, although Mo is much closer to the limit than W (figure 1(*b*)), it does not exceed the HSE γ-dose-rate limit beyond around 1 year after operation (figure 3(*c*)) in this simulation, and thus neither do the dose contributions from those individual radionuclides (or any other).

The highest activation and dose contributions at these long decay times comes from ^{91}Nb, which, in this simulation for the divertor armour, contributes between 60 and 80% of the activity at all decay times greater than 2 years and less than 1000 years (the limit of the simulations in this case)—as shown by the % contribution evolution curves [29] of the same simulation in figure 3(*b*) and 3(*d*) for activity and dose, respectively.

The reaction pathways to produce these five nuclides from natural Mo and the relative (%) production contribution of those pathways were automatically calculated by FISPACT-II during the irradiation simulation (a unique feature of the code [21]) and these are shown in table 1. Pathways for three

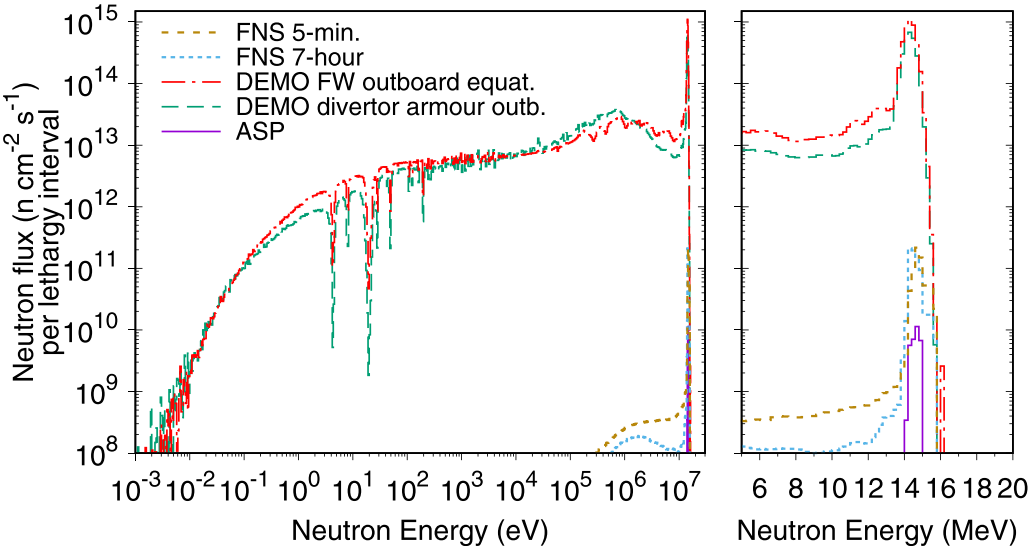

Figure 2. Simulated neutron spectra for the two different DEMO reactor locations: in the equatorial outboard (furthest from the centre) first wall and in the outboard region of the divertor armour. Spectra are also shown for conditions experienced by the thin, 25 × 25 mm^2 Mo samples in the FNS experiments, and the ASP spectrum calculated in [25] and used to irradiate Mo foils.

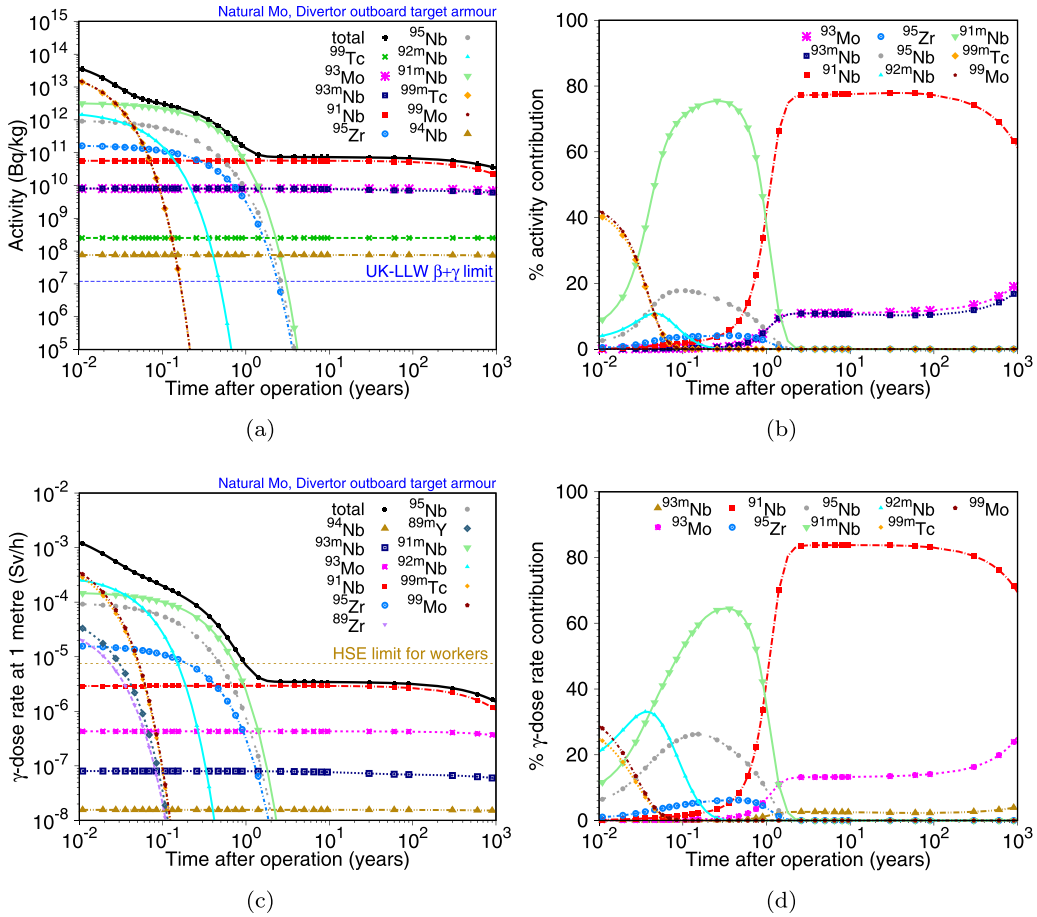

Figure 3. Radionuclide contribution curves to the activity and γ-dose in Mo predicted after a ~5-year exposure to the divertor armour spectra (figure 2). (*a*) Absolute activities, (*b*) % activity contributions, (*c*) absolute γ-dose-rates, and (*d*) % dose contributions.

Table 1. The primary generation pathways for the important radionuclides generated in natural Mo during exposure to the operating conditions expected for the outboard divertor armour of a typical DEMO concept. For each nuclide, the % contribution for each path corresponds to the results computed by FISPACT-II using TENDL-2019 nuclear data. Pathways here and in subsequent tables were identified using the tree-search algorithm employed in FISPACT-II, invoked via the UNCERT and LOOKAHEAD keywords—see [30] for more details.

Product	$T_{1/2}$	Pathways	Path %
^{99m}Tc	6.0 hours	^{98}Mo(n,γ)^{99}Mo(β^-)^{99m}Tc	55.4
		^{100}Mo(n,2n)^{99}Mo(β^-)^{99m}Tc	44.5
^{99}Mo	2.7 days	^{98}Mo(n,γ)^{99}Mo	55.4
		^{100}Mo(n,2n)^{99}Mo	44.5
^{91m}Nb	61 days	^{92}Mo(n,np)^{91m}Nb	94.5
^{93m}Nb	16 years	^{94}Mo(n,np)^{93m}Nb	68.2
		^{94}Mo(n,d)^{93m}Nb	21.3
		^{94}Mo(n,2n)^{93}Mo(β^+)^{93m}Nb	6.3
^{91}Nb	680 years	^{92}Mo(n,np)^{91}Nb	84.9[a]
		^{92}Mo(n,2n)^{91}Mo(β^+)^{91}Nb	14.2
^{93}Mo	3500 years	^{92}Mo(n,γ)^{93}Mo	22.0
		^{94}Mo(n,2n)^{93}Mo	77.5
^{94}Nb	20 000 years	^{94}Mo(n,p)^{94}Nb	75.3[c]
		^{95}Mo(n,np)^{94}Nb	24.2[c]
^{99}Tc	210 000 years	^{98}Mo(n,γ)^{99}Mo(β^-)^{99}Tc	55.4[b]
		^{100}Mo(n,2n)^{99}Mo(β^-)^{99}Tc	44.5[b]

[a]Includes contribution from the production (via the same path as the ground-state) and subsequent decay of ^{91m}Nb.
[b]Includes contribution from the production and decay of ^{99m}Tc.
[c]Includes contribution from the production and decay of ^{94m}Nb, $T_{1/2} = 6.3$ minutes.

shorter-lived nuclides—^{99m}Tc, ^{99}Mo and ^{91m}Nb—that contribute at least 40% to the total activity during decay times of less than 1 year (see figure 3(*b*)) are also included for reference (and are relevant for the experimental validation discussed later). Comparing these reaction chains to the isotopic abundance distribution of Mo (section 1.1) we can see that not all Mo stable isotopes are involved in the production of these dominant radionuclides. In particular, neither ^{96}Mo or ^{97}Mo appear in the table at all, and, moreover, the radionuclides with the three highest contributions to long-term activity in figure 3—^{93}Mo, ^{93m}Nb and ^{91}Nb—are produced almost entirely by reaction pathways from the two lightest stable isotopes of Mo; ^{92}Mo and ^{94}Mo.

1.3. Activation of individual Mo isotopes

The observation—that only some of the stable Mo isotopes cause high activation in Mo—is confirmed by the inventory simulation results of decay-activity and γ-dose in figure 4, where each Mo isotope has been separately exposed to the same DEMO divertor scenario as natural Mo (and W). As expected from the pathway analysis (table 1), ^{92}Mo and ^{94}Mo generate higher activity levels (figure 4(*a*)) at decay times greater than ~1 year than natural Mo because of the relative increase in production of the main problematic radionuclides discussed above. Meanwhile, the activity from monoisotopic Mo (probably not feasible, see below) composed of either ^{96}Mo or ^{97}Mo would actually satisfy UK-LLW limits on the desirable sub-100-year timescale in this DEMO scenario. Simulations for the remaining three isotopes (A = 95,98,100) predict activities above the LLW limit beyond 1000 years, but their activities are still 1–2 orders of magnitude below ^{92}Mo, ^{94}Mo and hence natural Mo beyond around 10 years of cooling.

The authors have previously [2] demonstrated a similar favourable result for ^{96}Mo or ^{97}Mo from the perspective of contact γ-dose-rate, which is confirmed by the present predictions for γ-dose at 1 m shown in figure 4(*b*) for the individual stable isotopes of Mo. As in [2], also note that ^{98}Mo and ^{100}Mo have relatively low γ-dose-rate beyond 10-years of cooling because the main long-lived radionuclide produced in them, ^{99}Tc (see table 1), is a not a γ-emitter.

1.4. Isotopic tailoring of Mo: a solution for fusion?

The results above suggest a solution that could make Mo more viable for fusion applications—instead of natural Mo, use Mo with an artificially adjusted (tailored) distribution of stable isotopes, preferably dominated by ^{96}Mo and ^{97}Mo (the exact level of enrichment towards these two isotopes would be defined based on a cost-to-benefit ratio) to reduce or prevent ILW. Previous work by Conn and Johnson [31] also identified ^{97}Mo as the most favourable isotope and their factor 100 reduction in radioactivity at 50 years for 99% ^{97}Mo agrees with the present findings. If Mo could instead be recycled, which is an attractive alternative to disposal [32] that is higher on the preferred waste management hierarchy [33], figure 4 demonstrates that isotopically-adjusted Mo would also have lower activation (and dose) on remote handling timescales ($< \sim 10$ years), potentially reducing reprocessing costs.

In the earlier work [31], it was recognised that the cost of isotopic adjustment must be balanced against the cost of radioactive waste disposal. Exact costs are difficult to quantify but basic storage of ILW is at least 10 times more costly per

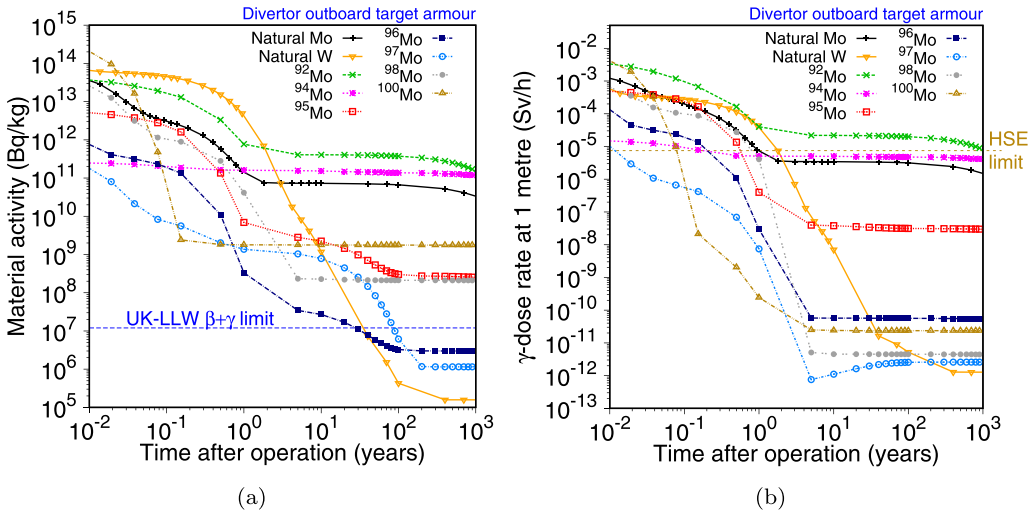

Figure 4. Simulation results Mo isotopes after a ~5-year exposure to the divertor armour spectra (figure 2). The post-operation activity in Bq/kg (*a*) and γ-dose-rate at 1 m in Sv/h (*b*) is shown as a function of time for different stable isotopes of Mo that have been individually exposed to a lifetime scenario for the outboard divertor target armour of DEMO (results for naturally occurring Mo and W are also shown for comparison). Notice the slight increase in γ-dose-rate in ^{97}Mo from around 4 years after operation, which is due to the feeding of ^{93m}Nb ($T_{1/2} = 16$ years) from the decay of the long-lived ^{93}Zr ($T_{1/2} = 1.5 \times 10^6$ years).

unit volume than LLW in the UK [34, 35], and this does not include the eventual cost of the final geological disposal facility (GDF) for ILW compared to a near surface LLW repository. The UK-GDF is predicted to cost ~£14 billion [34] and a fusion reactor would require a significant proportion of such a facility because of its typically larger expected size compared to equivalent fission plants; thus any reduction in ILW mass could be a significant cost saving.

A cost analysis must also consider the relative benefit of using Mo instead of W as an armour material; if a commercial reactor has much higher availability (or is viable at all) due to the choice of Mo, then greater profit margins could accommodate the higher cost of enriched Mo (compared to natural Mo). The amount of material required for the blanket and divertor armour is relatively small compared to the overall fusion power plant; in the DEMO model used in this work approximately 65 tonnes of Mo—replacing 120 tonnes of W—would be required, compared to, for example, ~ 4500 tonnes of in-vessel EUROFER [36] steel and more than 20 000 tonnes of 316 grade stainless steel in the reactor vacuum vessel. Even smaller amounts would be needed if Mo were only used instead of W for one application; for example, as a plasma-facing material in the divertor where the irradiation conditions, heat loads, and plasma interactions are the most severe (and thus where the benefit from any improved material performance would be greatest). Around 9 tonnes of Mo would be needed for the ~5 mm [11] thick armour layer of the divertor (compared to ~ 17 tonnes of W) in the DEMO model. In these contexts, it is not unfeasible to imagine a switch to Mo, even if the form of Mo required (isotopically tailored) is relatively expensive.

It is also worth noting that the political and public perception of nuclear waste has changed dramatically since the early days of fission. The political 'cost' of having Mo that can be disposed of as LLW in a near-surface waste repository instead of requiring deep-geological disposal for ILW (for which there is currently no solution in many countries, including the UK), could be the difference between gaining a nuclear license or not.

The current industrial standard for isotopic enrichment is via cascades in gas centrifuges and this has been explored for Mo [37], but is likely to always be prohibitively expensive (based on the estimates in [37] it could cost several $100 million to produce enough enriched Mo for the armour of a fusion reactor via gas centrifuges). A more detailed cost analysis is beyond the scope of this paper, but it is clear that new (or refined) industrial-scale separation techniques are needed to reduce the costs. A technique based on a free electron laser of CO_2 [38] has been explored for Mo, while electromagnetic separation [39, 40] is potentially a viable approach to achieve high enrichment of the middle mass range of Mo isotopes (*i.e.* the ones that would produce low activation Mo) and is the only viable method for isotope separation of many elements, including rare-earth metals [39].

Mo with a modified isotope distribution could also be useful to reduce the long-term activation and waste-disposal issues of convention ferritic/martensitic (F/M) steels, which are the fore-runners of the reduced-activation F/M (RAF/M) steels such as EUROFER [36, 41, 42] that is currently the preferred option for in-vessel fusion-reactor components for EU-DEMO [11, 43, 44]. T91 is an example of a F/M steel that is already widely used as a structural material in light-water reactors and in fossil-fuel plants, particularly in steam pressure vessels and boilers [45, 46], and thus is already manufactured at an industrial scale (unlike some RAF/M steels). However, in common with other F/M steels, T91 contains around 1 wt.% Mo. Based on previous work [47], it would cost around £1–2 million to use isotopically-tailored Mo at this concentration per 100 tonnes of steel. Even scaled to the several thousand tonnes of in-vessel steel required for current DEMO designs,

such costs are not unfeasible for devices costing many billions of Euros.

Mo also has potential applications as a structural material in fuel elements to improve safety in future generations of fission power plants [37, 48]. In this case, the barrier to realisation is the very high (thermal) capture cross section for neutrons in natural Mo, which is obviously undesirable when trying to create a sustained nuclear reaction. Once again, isotopic tailoring to reduce the problematic isotopes (in this case mainly ^{95}Mo, which has a capture cross section of 13.6 barns at a neutron energy of 0.025 eV [48]) offers a possible solution.

High neutron capture cross sections could also be a problem if Mo is used in significant concentrations in the tritium-breeding zone of fusion reactors, where the loss of neutrons in a material with a high absorption cross section could impact on the TBR (tritium breeding ratio) [49]. This might impact more severely breeding blanket concepts involving Li-Pb eutectic where satisfactory tritium breeding rates are reliant on high ^{6}Li enrichment (around 90% [11]). The ^{6}Li(n,α)^{3}H cross section is particularly high at low neutron energies and competing capture with Mo could therefore be detrimental.

Notice that in the divertor simulations (figure 4(*a*)) activity levels of pure ^{96}Mo or ^{97}Mo are relatively (compared to the much higher activity from other pure isotopes) close to the UK-LLW limit. Indeed, in the other case from figure 1(*a*), for the blanket first wall armour, even for these two isotopes the generated long-term activity (typically from longer reaction chains involving neutron multiplication, (n,2n) and/or neutron capture reactions to the same radionuclides shown in table 1) would exceed the LLW limit. Thus isotopic tailoring is unlikely to be a complete solution for the waste disposal of fusion components containing Mo (unless regulatory limits can be revised/relaxed for fusion waste [12]). However, isotopically adjusted Mo could be used in a 'mixed solution' with W, where W is used primarily in higher-flux first wall regions and therefore replaced more regularly, while Mo could be used as an armour in less exposed regions (e.g. in the divertor or away from the equator regions of the blanket), thus reducing the frequency with which those components need replacement (assuming Mo proved to be more resilient than W) and thereby reducing maintenance cycles and costs, and improving overall fusion plant availability.

Predictions such as those discussed in this simulation study rely on accurate nuclear code simulations. While the numerical techniques employed by inventory codes like FISPACT-II or neutron transport simulators like MCNP are well-established and validated (see e.g. [50, 51]), it is still the case that the quality and completeness of the underlying nuclear data strongly determines the reliability of predictions and the level of uncertainty; the latter could influence the level of conservativeness in engineering limits, which could impact on cost, and so there is a strong incentive to reduce uncertainty. Of particular importance for simulating the radiological response of Mo (or any other material) under fusion conditions is the accuracy of the integrated reaction rates that govern the production of dominant radionuclides. The remainder of this paper describes efforts at UKAEA to test and validate the nuclear reaction data used with FISPACT-II for Mo by benchmarking simulation results against both historical experimental decay-heat measurements and newly acquired γ-spectroscopy data.

2. Fusion decay-heat benchmark

At the end of the last century, JAEA used their 14 MeV fusion neutron source (FNS) facility to perform experiments on small material samples. The objective of the experiments undertaken by Maekawa *et al* [52–56] was to provide decay-heat data relevant to fusion systems that could be used to test the quality of nuclear simulations. This wealth of carefully obtained data has been used to validate inventory code predictions in the last two decades, but it was a relatively arduous and error-prone process until UKAEA's recent efforts [57] to construct a fully-automated simulation benchmark. A detailed description of the benchmark, including the experiments and the simulation approach with FISPACT-II, is provided in [57] and the most recent complete benchmark, covering more than 70 materials and focusing on validating FISPACT-II with the TENDL-2019 library, has been compiled into an openly accessible report [58]. Here, the discussion is focused on the comparison between simulations and the experimental measurements for Mo.

For Mo, thin metallic foil samples 25 $\times$ 25 mm^2 in area and approximately 10 μm thick, were irradiated for either 5 minutes or for 7 hours at fluxes of between 10^9 and 10^{10} n cm^{-2} s^{-1}. The reported decay-heat results by Maekawa *et al* were scaled to a flux of 10^{10} n cm^{-2} s^{-1} using the aluminium monitor foils that were included in each experiment to calibrate the neutron fluence based on γ spectroscopy of ^{24}Na produced via ^{27}Al(n,α)^{24}Na (similarly to the approach taken for ASP and described in [59]). Figure 2 shows the typical neutron spectra experienced by the samples in the 5-minute and 7-hour cases (different sample locations and hence different spectra—the 5-minute experiments used a rapid extraction system and associated set-up, which was not used in the 7-hour cases).

Decay-heat measurements at various cooling times after irradiation were obtained from a whole energy absorption spectrometer (WEAS), which detected both β^- and γ emissions with near 100% efficiency using a twin BGO (bismuth germanate) scintillator arrangement and a centrally located sample position to produce close to 4π steradians counting geometry [60]. For the 5-minute experiments, the rapid extraction system allowed the first measurements to occur within 1 minute of the end of irradiation and further measurements were taken for the next 1 hour. In the 7-hour case the first measurements did not take place until nearly 15 hours after the irradiation, but measurements were repeated for up to 200 days, allowing the contributions from radionuclides with longer half-lives to be captured.

Figure 5 shows the decay-heat measurements (as points) obtained for the two sets of Mo experiments (an earlier set of 5-minute irradiations of Mo are not included here for brevity, but are considered in [58]). Figures 5a and 5b, for 5-minute and 7-hour (*i.e.* a full day of irradiation

time at the FNS facility) irradiations, respectively, compare the experiments to FISPACT-II simulations (curves) of the total decay-heat performed with TENDL-2019 [23] nuclear data and several other major international nuclear libraries (see [57, 58] for details). In both cases there is very good agreement between the simulations and experiment, with *C/E* (calculated decay-heat divided by experimental measurement) values generally close to one, particularly with TENDL-2019, where *C/E* values lie in the range 0.97–1.01 for the 5-minute experiment and 0.9–1.4 in the 7-hour case [58].

In the 5-minute experiment the main radionuclide contribution to decay-heat is ^{91}Mo, produced via (n,2n) reactions on ^{92}Mo (see the pathway analysis for FNS in table 2), which contributes at least 70% of the simulated decay-heat throughout the 1-hour of experimental measurement time, as shown in the % contribution chart in the bottom panel of figure 5c. The upper panel of figure 5c shows the absolute nuclide contribution breakdown [29] and there are a number of other minor radionuclides predicted by the simulations, which are not important to capture the decay-heat from Mo for short, 5-minute irradiations and short, 1-hour cooling times.

In the longer, 7-hour experiment, the nuclide breakdown from the TENDL-2019 simulation (figure 5d) suggests a more complicated picture, with a number of different radionuclides providing significant contributions to the total decay-heat at different times during the ~ 200 days of cooling time where experimental measurements were recorded. In the first week of cooling ^{99}Mo dominates, but as this nuclide decays with a half-life of 2.7 days (see table 2), by around 20 days of cooling it is replaced by three unstable nuclides of Nb with longer, 10-60 day half-lives: ^{92m}Nb, ^{95}Nb, and ^{91m}Nb. This relatively complex radiological landscape is a very good match to the experimental measurements—as demonstrated by the absolute nuclide breakdown plot, where the combination of decay-curves for these four nuclides produces a very good match to the time-evolution profile of the experiment. Such close agreement to experiment in such a complex case demonstrates the efficacy of the FISPACT-II system, including the computational method, and confirms the validity of the underlying nuclear data.

The pathway analysis for these simulated experiments in table 2 shows the major production routes for the five important radionuclides for FNS experiments on Mo. The cross sections (primarily for 14 MeV neutrons—see figure 2) of a number of different non-elastic reactions, such as (n,2n) [neutron multiplication] and (n,p) [neutron capture, proton emission], on several isotopes of Mo are tested (and validated) by this experimental benchmark for Mo. Included in the validation are some reactions that are predicted to be important for the activation of Mo in a fusion reactor (compare tables 1 and 2), such as those producing ^{99}Mo and ^{91m}Nb. However, as expected, the experiments do not provide any useful data to test the production of the long-lived radionuclides that would cause disposal and handling problems for Mo components.

3. ASP experiments

From 2011–2015 [59, 61–64], in an effort to improve the quality of experimental reaction cross section data for fusion-relevant materials at fusion-relevant neutron energies, UKAEA undertook a series of 14 MeV neutron irradiation experiments at the experimental facility known as 'ASP', which is hosted at AWE Aldermaston in the UK. The aim of the experimental campaigns was to gain additional cross section data-points at 14 MeV for reactions where data was deficient—this is true for many important reactions for fusion materials [65, 66]—and thus to aid the evaluators working on the next generation of nuclear data libraries by providing more information with which to fit the theoretical models that generate continuous cross section curves.

The experimental set-up (figure 6) involved an accelerated deuteron beam impinging onto a tritium-loaded target to produce a source of 14 MeV neutrons (via DT reactions), which was then used to irradiate a wide variety of material foils. After irradiation the foils were transferred rapidly via a pneumatic extraction 'Rabbit' tube to a high-purity germanium (HPGe) γ-detector and the full time evolution in the energy-count profile of γ emissions from the activated material was recorded. Full details of the experimental approach are given in [61–62]. More than 300 separate experiments were performed, generating more than 10000 separate γ spectra (the integral spectrum of γ counts is recorded at multiple time intervals for each experiment to enable analysis—see below), and previous efforts [59] to process such large data sets in a rigorous, consistent and automatic manner are still ongoing [25]. In the present work, we instead, focus on analysing eight experiments involving samples of Mo.

Figure 7 shows the typical raw data obtained from the ASP experiments, along with plots showing the different stages of the analysis approach. The data shown corresponds to experiment 82 in UKAEA's campaign, which included a Mo foil. The full, time-integrated γ-spectrum (figure 7(*a*)) recorded for 15 minutes after irradiating the foil triplet of Mo-Fe-Al shows various peaks at characteristic γ-energies for different radionuclides produced in the foils during the ~5-minute irradiation (both the irradiation time and measurement time varied between experiments, but was accurately recorded). The main peaks, which have an almost Gaussian profile, are centred on discrete γ-emission lines and are highlighted in the figure, including the electron–positron annihilation peak at 511 keV, the potassium-40 (^{40}K) organic background signal at 1461 keV, and various peaks associated with radionuclides produced during irradiation in the Mo, Fe and Al foils.

3.1. Flux estimation

Fe and Al foils were included in the experiments to enable accurate measurement of the neutron flux received at the sample location during irradiation [59]. In the present work, the major lines from ^{27}Mg at 844, 1014 and 171 keV, ^{24}Na lines at 1369 and 2754 keV due to Al activation, along with ^{56}Mn (produced in the Fe foil) lines at 847, 1811 and 2113 keV, were used to produce an average estimate of the

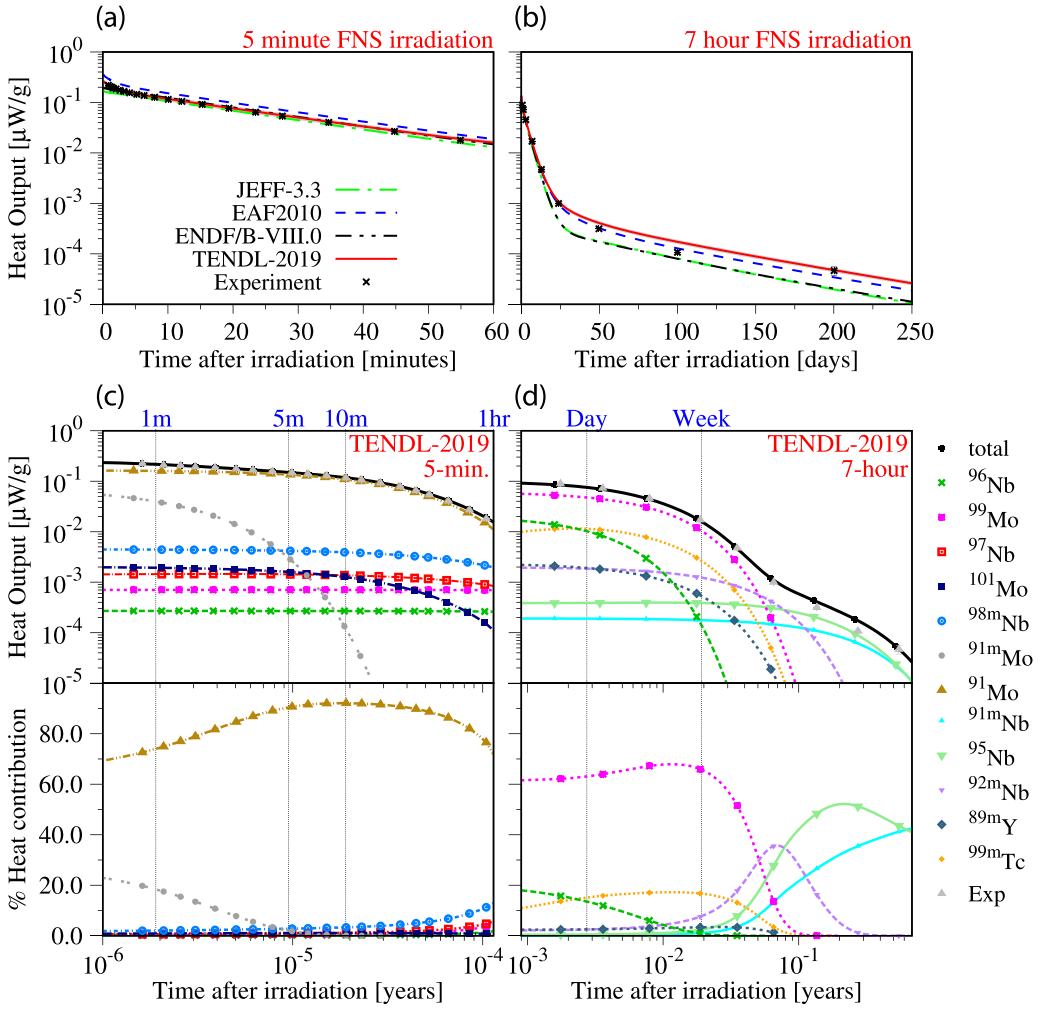

Figure 5. Simulation & experimental decay-heat results from the FNS benchmark for Mo. (*a*) and (*c*) correspond to decay-heat following 5-minute irradiations, (*b*) and (*d*) are the equivalent data after 7-hour irradiations. (*a*) and (*b*) show total decay-heat curves on linear time-after-irradiation scales for the different nuclear library simulations with FISPACT-II, the experimental measurements as points with vertical lines showing experimental uncertainty, and the nuclear-data-uncertainty band (in grey) for the TENDL-2019 [23] library. (*c*) and (*d*) present the radionuclide breakdown of contributions to the total decay-heat from the TENDL-2019 simulations in absolute μW/g terms (top halves) and as % contributions (bottom halves)—on logarithmic time-after-irradiation scales.

Table 2. List of contributing reaction-route pathways for the important radionuclides identified by FISPACT-II in simulations of the FNS experiments on Mo.

Product	$T_{1/2}$	Mo FNS experiment	Pathways	Path %
^{91}Mo	15.49 min.	5-min.	^{92}Mo(n,2n)^{91}Mo	100.0[a]
^{99}Mo	2.7 days	7-hour	^{100}Mo(n,2n)^{99}Mo	99.6
^{92m}Nb	10 days	7-hour	^{92}Mo(n,p)^{92m}Nb	100.0
^{95}Nb	35 days	7-hour	^{95}Mo(n,p)^{95}Nb	86.8
			^{96}Mo(n,d)^{95}Nb	6.9
			^{96}Mo(n,np)^{95}Nb	5.6
^{91m}Nb	61days	7-hour	^{92}Mo(n,np)^{91m}Nb	94.0
			^{92}Mo(n,2n)^{91m}Mo(β^+)^{91m}Nb	3.7
			^{92}Mo(n,d)^{91m}Nb	2.3

[a]Includes contribution from the production and isomeric transition (IT) decay of ^{91m}Mo, $T_{1/2} = 1.1$ min.

neutron flux for each experiment. Note that for experiment 81, a transfer issue meant that the acquisition data (counts) from the aluminium foil were not properly recorded and so the flux estimate is based solely on the ^{56}Mn peaks in this case. Table 3 gives the details of the eight experiments considered here for Mo, including the results of the Fe/Al-foil flux estimates. % error estimates for the flux evaluations are based on the standard error (*i.e.* the deviation from the mean) of the average

Table 3. Experimental details and flux estimates for the ASP experiments involving Mo.

Experiment	Material masses (g)			Irradiation	Estimated flux	
number	Mo	Fe	Al	time (min.)	(n cm^{-2} s^{-1})	error (%)
81	0.151 9	0.106 6	N/A[b]	5	8.7×10^8	11.3
82	0.152 9	0.105 4	0.038 2	5	9.3×10^8	11.1
111	0.155 8	0.106 3	0.038 5	5	6.6×10^8	12.7
112	0.155 1	0.106 7	0.038 9	4.67	6.8×10^8	13.5
134	0.461 1[a]	0.106 2	0.038 4	60	4.2×10^8	10.3
226	0.153 9	0.110 4	0.036 2	10	2.5×10^8	18.1
244	0.151 8	0.110 5	0.028 9	30	3.6×10^8	15.4
284	0.153 7	0.111 1	0.029 3	30	8.4×10^8	14.8

[a]Three Mo foils were used in a stack for this longer irradiation experiment.
[b]Experimental issue, see main text for details.

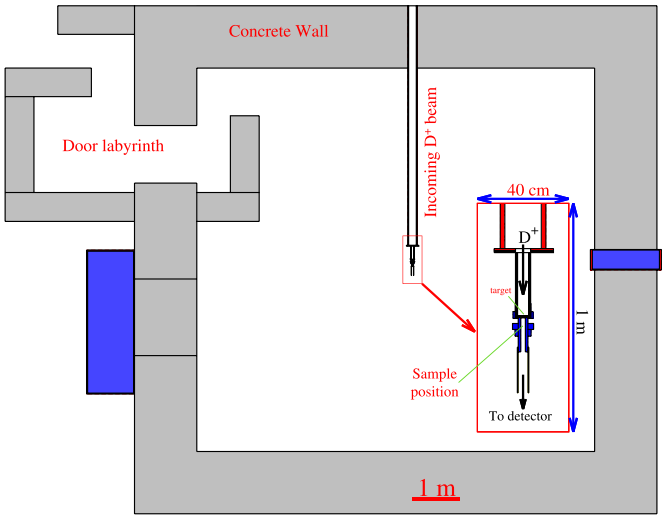

Figure 6. Simplified ASP geometry (used in MCNP calculations) showing chamber walls and labyrinth exit (in grey) and a close up of the target geometry, where the incoming D^+ deuteron beam is accelerated onto the tritium target, which is adjacent to the sample chamber (in blue). Samples are inserted and extracted (to the γ detector) from this chamber via a pneumatic Rabbit tube.

flux estimates summed in quadrature with each individual flux estimate multiplied by the fractional Poisson statistical uncertainty ε in the background-corrected γ-counts for the associated peak:

$$\epsilon = \sqrt{C_p + C_B}/C_p^*, \tag{1}$$

where C_p is the raw total count in the detector channels containing the peak of interest, C_B is the total background count subtraction for the peak channels (*i.e.* via figure 7(*b*)), and C_p^* is the total background-corrected count for the peak ($\equiv C_p - C_B$). For further discussion of the application of Poisson statistics to radioactive decay and γ-spectroscopy, see [67–69].

The flux estimation was done using the Levenberg–Marquardt algorithm (LMA—a damped least-squares method) to fit a decay function to the counts per (real) time (in seconds), and hence to calculate decay-corrected A_0 values for the end of irradiation activity in Bq. Note that in all cases the fitting was only performed out to a maximum of three times the half-life of the nuclide being analysed, thereby avoiding any problems in the fit that could be caused by including very small counts at long decay times (for that particular nuclide). It is also possible for the peaks of two different radionuclides to overlap sufficiently so that their individual counts cannot be separated from one-another. In the present work, this situation only occurred for the 847 and 844 keV peaks of ^{56}Mn and ^{27}Mg, respectively, and in this case, as described in [59], a double exponential fit is performed to obtain the two separate A_0 activities.

In calculating the flux using these reference foils, it is assumed that the reaction pathways (see table 4) to the measured nuclides are well-known and that the nuclear cross section data (from TENDL-2019 [23]) is well-validated. The cross section vector for each reaction is 'folded' (vector dot product) with a normalised ASP neutron irradiation spectra (calculated using a Monte Carlo simulation as part of the work described in [25] and shown unnormalised in figure 2) to calculate the average cross section σ in barns for the ASP spectrum. Using the standard decay equations describing the production and decay of radionuclides [70], A_0, σ and the decay constant λ are used to estimate the experimental flux via:

$$\phi = \frac{A_0}{N\sigma(1 - \exp^{-t_{\rm irr}\lambda})}, \tag{2}$$

where $t_{\rm irr}$ is the irradiation time of the experiment (given in table 3) and N is the total number of atoms of the target (stable) nuclide—in this case of ^{56}Fe or ^{27}Al. Note that this approach is only valid if the neutron flux is approximately flat (constant) during the irradiation. The flux profile was monitored during each experiment and adjustments to the deuteron beam were made in real-time to maintain a near-constant flux profile; which was confirmed *posteriori* by the output of a pair of fission counters that monitored the neutron count near to the ASP target (but were not close enough to provide a reliable measurement of the flux on the samples).

The estimated fluxes are used as input to FISPACT-II inventory simulations to obtain a calculated C activity—see section 3.3.

3.2. Experimental activity *E*

For the experimental value E, the first stage is to extract the detector counts for each detectable γ-peak of the γ-emitting

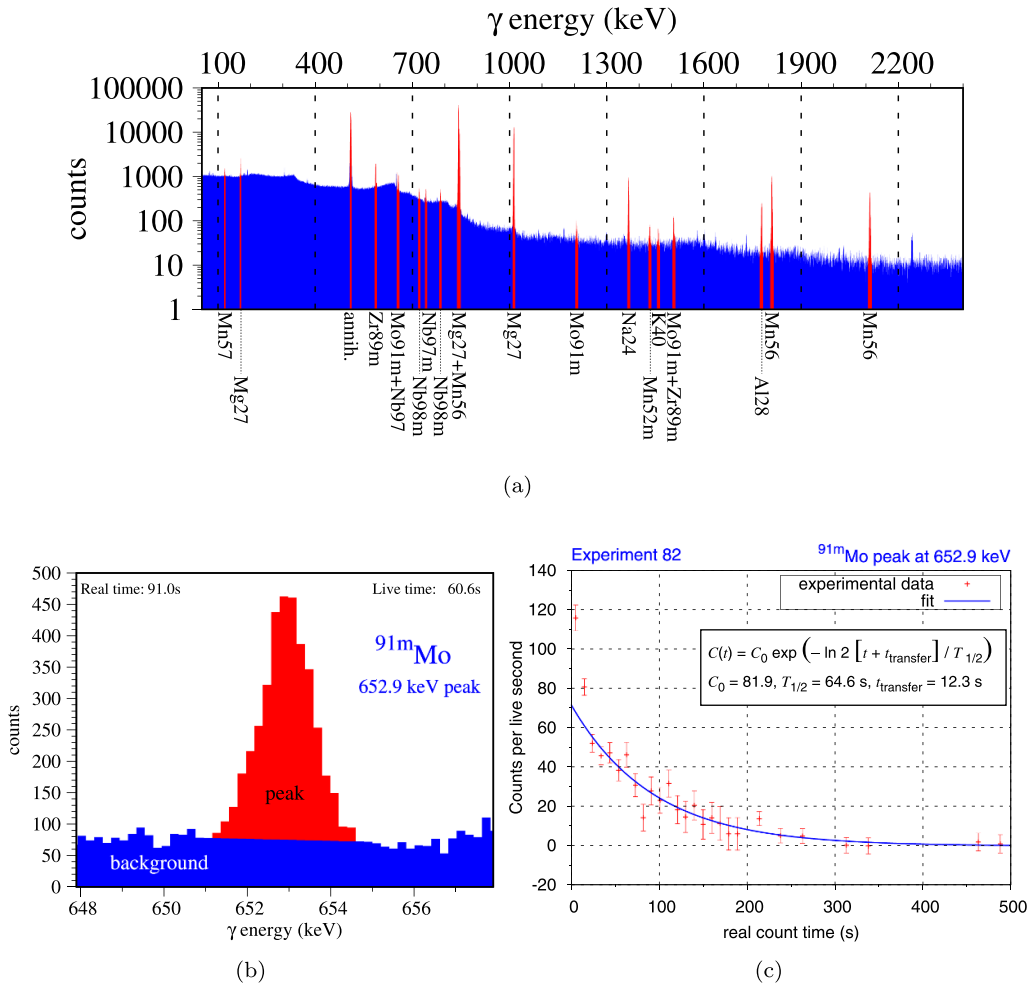

Figure 7. Experiment 82 γ spectroscopy. (*a*): final (end of ~ 15-min. acquisition) integrated γ spectrum. (*b*): 652.9 keV peak associated with ^{91m}Mo after 91 s, showing the peak area after subtraction of the background. (*c*): counts as a function of time for this peak (with count statistical error bars) and the curve fitted to the data (see main text for details). C_0 is the dependent (free) variable. t_{transfer} is the time delay between the end of the irradiation and the start of the γ-data acquisition (typically ~ 10 s).

radionuclides produced during the irradiation of Mo at ASP. Peaks associated with five different radionuclides were identified in the present work; these are listed in table 4 (along with flux-estimator nuclides of Fe and Al), together with their half-lives, and main production pathways according to FISPACT-II simulations with TENDL-2019 for the irradiation time and flux-estimate associated with experiment 82 (see table 3). The identifiable peaks for each radionuclide are listed in table 4 and are labelled in the integral spectrum for experiment 82 (figure 7(*a*)).

Figure 7(*b*) demonstrates the process by which the background counts (mainly from Compton scattering since the detector was well shielded using lead) are subtracted, using linear interpolation between the average counts recorded in a range of channels on either side of a peak [59], to give the counts associated with the decaying nuclide—in this case for ^{91m}Mo associated with its γ line at 653 keV. Note that the background subtraction exemplified in figure 7(*b*) only applies to peaks (or peaks in overlap scenarios) that are away from the Compton edge [70], which was true for all peaks considered in the present work. The fit to the resulting evolution in counts-per-live-second as a function of (real) time for a peak (e.g. as in figure 7(*c*) for the ^{91m}Mo peak) then gives the experimentally predicted count rate at the end of irradiation C_0, which in turn is used to calculate A_0 via

$$A_0 = \frac{C_0}{D^{\text{eff}}(E_p^{\gamma})I_p}, \tag{3}$$

where $D^{\text{eff}}(E^{\gamma})$ is the detector efficiency at γ-energy E^{γ}, which for the HPGe detector used in the present work is described by a function fit to neutron transport simulations performed on a model of the detector (e.g. as described in [25]). E_p^{γ} and I_p are the energy and intensity of peak p, respectively, both taken from `decay_2012` decay-data files used by FISPACT-II [21] for TENDL-2019.

3.3. Calculated activity *C*

The calculated (C) estimate of A_0 is taken directly from a FISPACT-II calculation with the TENDL-2019 data library. The appropriate mass of pure Mo was irradiated for the experimental irradiation time at the estimated flux (section 3.1) and

Table 4. Information about the radionuclides measured in the ASP experiments. The FISPACT-II-calculated production pathways and their % contributions were obtained from the simulations with the TENDL-2019 library. Only the γ-peak energies observed in the experiments are listed for each nuclide.

Product	$T_{1/2}$ experiment	Pathways	Path % TENDL-2019 (Exp. 82)	Experimentally identifiable γ-peaks (keV)
^{56}Mn	2.58 hours	^{56}Fe(n,p)^{56}Mn	100.0	846.8, 1810.7, 2113.1
^{27}Mg	9.46 min.	^{27}Al(n,p)^{27}Mg	100.0	170.9, 843.7, 1014.4
^{24}Na	14.96 hours	^{27}Al(n,α)^{24}Na	100.0	1368.6, 2754.0
		^{97}Mo(n,p)^{97m}Nb	83.7	
^{97m}Nb	53.0 s	^{98}Mo(n,np)^{97m}Nb	2.1	743.4
		^{98}Mo(n,d)^{97m}Nb	14.1	
^{91m}Mo	1.08 min.	^{92}Mo(n,2n)^{91m}Mo	100.0	652.9, 1208.1, 1508.0
^{89m}Zr	4.13 min.	^{92}Mo(n,α)^{89m}Zr	100.0	587.8
^{98m}Nb	51.30 min.	^{98}Mo(n,p)^{98m}Nb	100.0	722.6, 787.4
		^{97}Mo(n,p)^{97}Nb	81.5[a]	
^{97}Nb	1.23 hours	^{98}Mo(n,np)^{97}Nb	12.1[a]	657.9
		^{98}Mo(n,d)^{97}Nb	6.3[a]	

[a]Includes contribution from the production and isomeric transition (IT) decay of ^{97m}Nb, but note that different reactions have different probability ratios between ground- and meta-state production (*i.e.* the distribution of production % values for ^{97m}Nb are different to those of ^{97}Nb).

using the calculated neutron spectrum for the sample location shown in figure 2 (the mass, flux-estimate, and irradiation times for each experiment are given in table 3). FISPACT-II automatically outputs the individual radionuclide contributions to the total sample activity, and the required end-of-irradiation values can be easily extracted for the specific nuclides.

3.4. ASP results

Figure 8 shows *C*/*E* ratios for the calculated (*C*) and experimental (*E*) A_0 activities for the eight Mo experiments. ^{97}Nb and ^{97m}Nb results are plotted in the same panel, while the other three panels in the figure show results for single radionuclides (as labelled). Tables B1 and B2 in the appendix give the numerical *C*, *E*, *C*/*E* values for each data peak. The error estimates on each value, shown as error bars in the figure (and also provided as percentages in the tables), include, for *C* values, the error of the flux estimate (see table 3) and the error calculated by FISPACT-II using the uncertainty data in TENDL for the relevant cross sections (e.g. as shown in the grey error bands of the cross section figures in figure A1 of the appendix) summed in quadrature, and for *E*, the activity error based on the Poisson count uncertainty (equation (1)). These uncertainties should be refined to account for other (potentially systematic) errors and correlations, such as uncertainty in the experimental timing information, but not all of this information is available from the experiments, so the present estimates (potentially pessimistic) are the best available and give and indication of the error magnitudes. The lessons learnt in this work will help to inform better experimental methodology with respect to uncertainty quantification in future campaigns.

Note in figure 8 that not every experiment has produced a *C*/*E* value for every possible peak considered. Peaks with total background-corrected counts of less than 400 during the entire measurement time were deemed to be of low statistical quality and were omitted. Also shown for each panel, as a visual guide to the data trend, is the weighted average *C*/*E* value, where the weights correspond to the inverse of the variance (square of the error) for each point. The standard deviation from these weighted averages is shown by the grey band in each plot.

3.4.1. ^{89m}*Zr* . The results are consistent for ^{89m}Zr, with *C*/*E* just below one for almost all experiments and with small uncertainties generally including one within their range. Only experiment 134 produces a discrepant result for this radionuclide—as it does for other nuclides considered—but this does not alter the overall agreement; as demonstrated by a weighted average *C*/*E* just below one and small spread of values about this mean.

The irradiation time in experiment 134 was 1 hour; longer than usual for these experiments (see table 3), and the detector measurements were extended to an over-night count. Three Ti foils were also included in both the irradiation and counting stack, which also included three Mo foils instead of the usual one. The combination of increased irradiation time, leading to higher production of longer-lived (compared to the nuclides being analysed) radionuclides, and interference from radionuclides produced in Ti, have caused the peaks from the radionuclides of interest to have more background counts, a higher signal-to-noise ratio, and thus lower overall counts than expected—leading to an underestimate from the experiment and high *C*/*E* results. For example, the background count adjacent to the ^{89m}Zr at 588 keV is approximately three times higher in experiment 134 compared to experiment 111. In more carefully designed experiments the irradiation times should be tuned to best match the half-lives the nuclides-of-interest—this was not possible in the experimental campaigns performed so far, but is an area of future improvement.

The slight under-prediction in ^{89m}Zr production apparent from these results is worth noting, but the origin is uncertain—the cross section curve from TENDL-2019 for

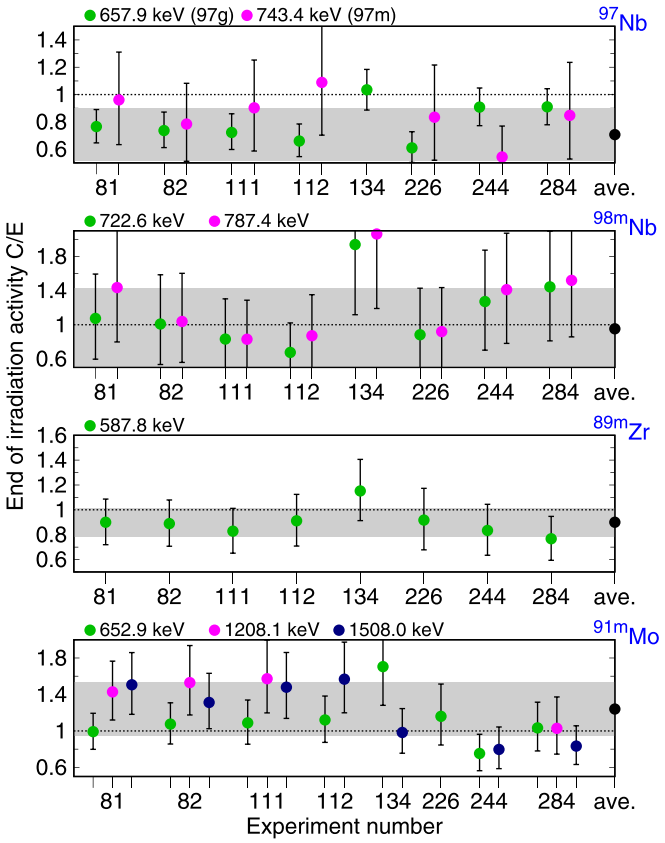

Figure 8. The complete set of *C*/*E* values calculated for the ASP experiments involving Mo foils. The colour of a point indicates which γ-peak it is associated with (listed at the top of each panel). Points are grouped by experiment along the *x*-axis. Each panel corresponds to the peaks of a different radionuclide, except for the top panel, where the single measured peaks from each of ^{97}Nb and ^{97m}Nb are shown together. The weighted-average *C*/*E* value for all peaks in each pane is also plotted in black, and the grey band behind the data represents the standard deviation of the *C*/*E* values from this average.

^{89m}Zr production from ^{92}Mo (figure A1(*c*) in the appendix) on the contrary appears to be slightly above the bulk of EXFOR [71] data points, which would instead suggest an overproduction of ^{89m}Zr in calculations. Further experiments are warranted and should be targeted specifically at ^{89m}Zr production.

3.4.2. ^{91m}Mo. *Only* the lowest energy peak at 653 keV produces consistently good *C*/*E* values—both close to one and with small uncertainties (with one within the uncertainty range). 653 keV is the highest intensity peak ($I_p \approx$ 0.5). The other, higher-energy peaks for this radionuclide have lower intensities and thus produce smaller count-rates in the experiments—the 653 keV peak integral typically comprised 2000-4000 counts for this nuclide, while the other two produced a maximum of around 700 counts each (some counts were even below the 400 threshold discussed above). This may explain the discrepancy observed in figure 8. On the other hand, figure A1(*a*) in the appendix, comparing the TENDL-2019 cross sections to the differential experimental data (*i.e.* cross section values at single energies) available in the international EXFOR database [71] for the (n,2n) reaction that produces ^{91}Mo, does suggest a slight overestimation for the path to the metastable 91m; the TENDL curve at 14 MeV is higher than the majority of the differential data. However, the result from the present work is not conclusive enough to make a recommendation for future TENDL evaluations.

3.4.3. ^{98m}Nb. Apart from experiment 134, for the reasons outlined earlier, *C*/*E* results for ^{98m}Nb are relatively consistent for the two different peaks identified in each experiment, although there is a large spread between experiments. The errors are also larger compared to the results for other nuclides, which is caused by the large nuclear data uncertainties in TENDL-2019 for the (n,p) reaction producing this nuclides from ^{98}Mo—as shown in figure A1(*d*). Looking closely at that plot for TENDL-2019, which has changed significantly compared to TENDL-2017 [72], one can see an evaluation for the reaction channel to ^{98m}Nb that is influenced by a large spread of data points, particularly around 14–15 MeV, but the overall TENDL-2019 curve appears higher than the bulk of the experimental data points. This would tend to suggest an overprediction of the production of ^{98m}Nb, but the experimental finding in the present work are not conclusive in this respect. The results indicate the need for further experiments on this reaction and an analysis of the evaluated curves in TENDL-2019.

3.4.4. ^{97}Nb and ^{97m}Nb. Results for ^{97}Nb and ^{97m}Nb (one peak each) also show consistency within each experiment, but the calculated values appear to underestimate the production of these two nuclides; for several of the *C*/*E* values even their uncertainty range does not include one (indicating significant deviation between calculation and experiment). The weighted average *C*/*E* is around 0.8 and the deviation from this average does not include one. There is nothing conclusive in the comparison of TENDL-2019 to EXFOR in this case (figure A1(*b*)); if anything the TENDL cross sections for the primary (n,p) reaction (see table 4) producing ^{97}Nb appear to slightly underestimate the data at 14 MeV compared to EXFOR. The results for these nuclides need further investigation—probably involving additional experiments.

3.5. ASP summary

Considering all of the experimental uncertainties the fact that many of the *C*/*E* values are close to one (and all are less than 2), and that in many cases the uncertainties encompass one, is encouraging and demonstrates that the FISPACT-II calculations with TENDL-2019 produce good predictions for irradiation-induced activity in Mo in these scenarios. However, it is worth observing that, in contrast to the FNS benchmark (section 2), none of the reaction pathways interrogated by these experiments are relevant for the dominant channels to isotopes identified in the earlier fusion power plant scenario (compare table 4 to table 1). Experiments involving measurement of such long-lived reaction products will likely require longer irradiations and post-irradiation measurements.

For long-lived nuclides, including the important ^{91}Nb, ^{93}Mo, and ^{93m}Nb, the dominant production cross sections can have high uncertainty (e.g. the (n,np) channel responsible for the majority of ^{93m}Nb production has a nuclear data uncertainty greater than 50% in TENDL-2019 [23] under the ASP neutron spectrum). This demonstrates the need for future experiments with careful design; *i.e.* to ensure that the important reaction pathways are explored and that the resulting benchmark is as relevant as possible for Mo in a fusion power plant.

4. Conclusions

Inventory calculations with FISPACT-II have highlighted the issues surrounding long-term high-activation of Mo if it were to be used as an armour material in fusion systems. However, the simulations predicted that specific stable isotopes (^{96}Mo and ^{97}Mo) from Mo's wide distribution have lower activity and thus isotopic enrichment or bias towards these nuclides could produce a more acceptable material. Of course, this necessitates an isotopic separation method that is economically feasible compared to, in particular, the waste handling costs of using standard or natural Mo, or to the cost of potentially reduced component lifetime if W remains the default choice.

In parallel, it is important to have confidence in these simulated radiological responses, especially if they are going to be used—in the case of Mo—to make potentially expensive engineering design decisions for future fusion experiments and prototype power plants. Two experimental validation efforts for nuclear inventory code predictions of 14 MeV-neutron-induced activity in Mo have shown that the simulation methodology (FISPACT-II) and underlying nuclear data are reasonably successful. Using several international nuclear data libraries, FISPACT-II was able to accurately simulate decay-heat measurements obtained for Mo after exposure to 14 MeV neutrons for either 5 minutes or 7 hours in JAEA's defunct FNS facility. Additionally, γ-spectroscopy-derived activation estimates for radionuclides produced in Mo foils irradiated at the ASP 14 MeV-neutron source in the UK have provided a wealth of new data to test code predictions against. For Mo, eight separate experiments were used to derive end-of-irradiation activities for five different short-lived (half-life $T_{1/2} < 2$ hours) radionuclides with detectable γ-emissions. Comparison to simulations of the experiment, performed by FISPACT-II [21] with the TENDL-2019 [23] library, revealed a good agreement despite the large degree of uncertainty and sub-optimal experimental design.

These two benchmarks improve confidence in some aspects of code predictions for Mo in a fusion environment but further validation is required, particularly for the production of radionuclides expected to dominate activity in Mo for cooling times greater than ~ 1 year after exposure to typical demonstration fusion-reactor (DEMO) conditions; namely ^{91}Nb, ^{93}Mo, and ^{93m}Nb. The short irradiation timescales associated with the experiments discussed here prevent detailed interrogation and testing of the production routes of these long-lived radionuclides ($T_{1/2}$ ranging from decades, centuries to millennia). Further experiments, involving longer irradiations and/or higher neutron fluxes, are required, potentially in combination with improved γ-spectroscopy, such as extended recording times under very-low background conditions (e.g. underground systems like that available at Boulby in the UK [73]), or even alternative measurement approaches, such as coincidence counting systems (see e.g. [74, 75]) to detect positron emissions (e.g. for ^{91}Nb) or via mass spectroscopy for low concentration nuclides [76, 77].

However, longer-irradiation experiments are difficult to arrange in most existing facilities. There are several proposals being developed around the world to provide more favourable and dedicated fusion-relevant experimental conditions (e.g. IFMIF-DONES [78]). The urgency to deliver such facilities (or alternative, lower-cost options more targeted at nuclear data) will only increase in the next few decades as fusion moves away from a research focus to a more engineering realisation phase with DEMO and the other near-commercial devices planned.

Only with additional experiments of the kind described in this paper, targeted at fusion-relevant conditions for operational and decommissioning timescales, will there be sufficient data available to validate predictions for Mo and hence prove its viability (or not) as a candidate fusion reactor material; either in pure form or as part of an alloy, and whether it can be used with its natural isotopic abundances or if tailoring is required. In particular, serious effort to develop industrial-scale isotopic tailoring solutions for Mo (or other fusion materials) can only be justified if there is high confidence (low uncertainty) in code predictions.

Acknowledgment

This work was funded by the RCUK Energy Programme [grant number EP/T012250/1]. To obtain further information on the data and models underlying this paper please contact PublicationsManager@ukaea.uk.

Appendix A. Reaction cross section graphs

Figure A1 compares TENDL-2019 [24] cross sections to the international database of differential cross section data, EXFOR [71], for the reactions predicted by FISPACT-II to be responsible for the majority (see table 4) of the production of each of the four radionuclides detected in the ASP experiments on Mo. Curves of total cross sections, and the partials to ground and metastable states of each daughter nuclide are shown, and the EXFOR data is also separated by daughter state, subject to the data files from EXFOR containing enough data to make that determination (otherwise the default is 'total').

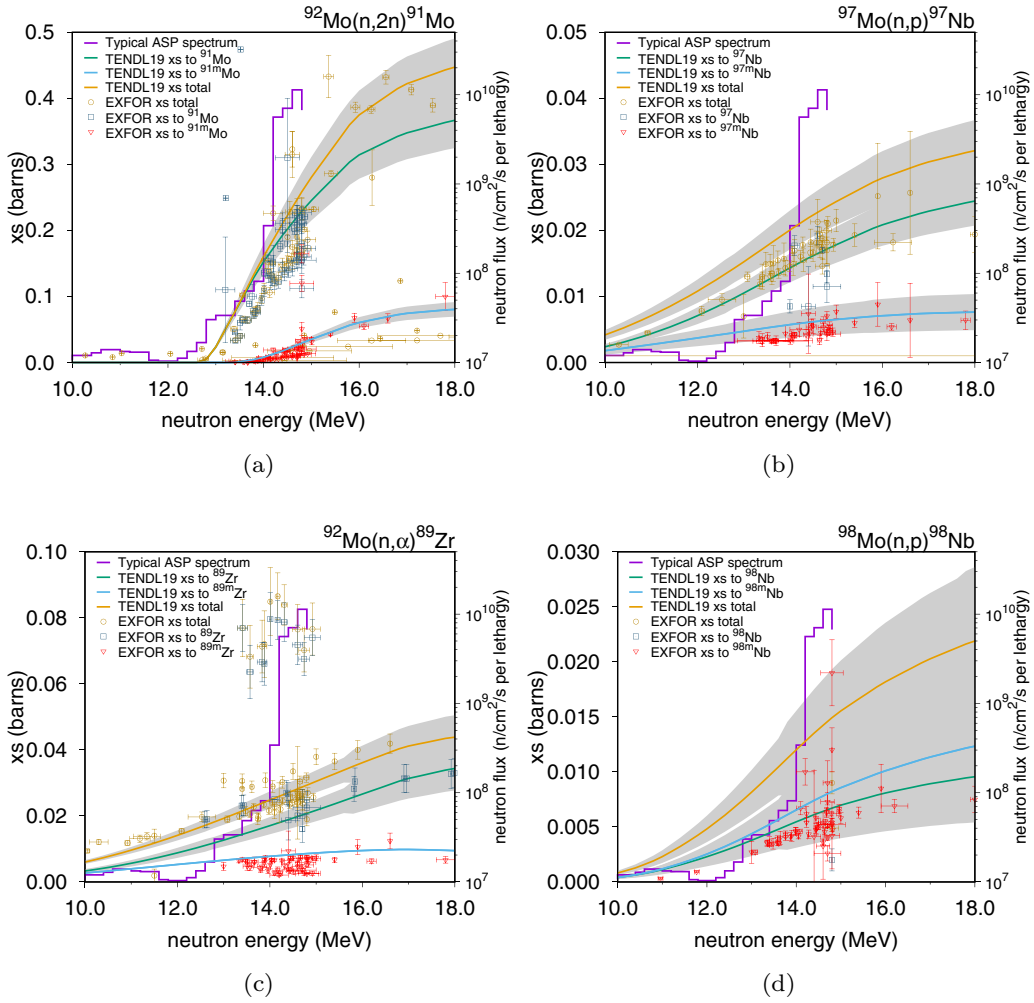

Figure A1. TENDL-2019 reaction cross sections and EXFOR differential data for the main reactions analysed by the ASP experiments on Mo. TENDL-2019 curves are accompanied by their corresponding uncertainty bands (in grey).

Appendix B. ASP experiments calculated and measured activities

Table B1. Calculated and experimental activities for ^{91m}Mo, ^{89m}Zr and ^{98m}Nb peaks measured in the ASP experiments.

Nuclide	Experiment number	Peak energy (keV)	Activity (Bq)		C/E	Error (%)
			Calc.	Exp.		
^{91m}Mo	81	652.9	2.13E+03	2.14E+03	0.99	20.1%
		1208.1	2.13E+03	1.49E+03	1.43	17.2%
		1508.0	2.13E+03	1.41E+03	1.51	16.4%
	82	652.9	2.29E+03	2.13E+03	1.08	19.8%
		1208.1	2.29E+03	1.49E+03	1.53	18.6%
		1508.0	2.29E+03	1.74E+03	1.31	18.8%
	111	652.9	1.67E+03	1.53E+03	1.09	20.7%
		1208.1	1.67E+03	1.06E+03	1.57	18.5%
		1508.0	1.67E+03	1.13E+03	1.48	18.3%

Table B1. Continued.

Nuclide	Experiment number	Peak energy (keV)	Activity (Bq)		C/E	Error (%)
			Calc.	Exp.		
	112	652.9	1.70E+03	1.51E+03	1.12	20.6%
		1508.0	1.70E+03	1.08E+03	1.57	17.6%
	134	652.9	3.23E+03	1.89E+03	1.70	20.2%
		1508.0	3.23E+03	3.29E+03	0.98	25.3%
	226	652.9	6.48E+02	5.59E+02	1.16	25.6%
	244	652.9	9.31E+02	1.24E+03	0.75	33.5%
		1508.0	9.31E+02	1.17E+03	0.80	34.1%
	284	652.9	2.18E+03	2.11E+03	1.03	25.2%
		1208.1	2.18E+03	2.12E+03	1.03	29.9%
		1508.0	2.18E+03	2.62E+03	0.83	29.6%
^{89m}Zr	81	587.8	4.93E+02	5.47E+02	0.90	22.5%
	82	587.8	5.30E+02	5.96E+02	0.89	23.3%
	111	587.8	3.87E+02	4.68E+02	0.83	26.0%
	112	587.8	3.79E+02	4.16E+02	0.91	24.8%
	134	587.8	1.28E+03	1.11E+03	1.15	19.0%
	226	587.8	2.08E+02	2.27E+02	0.92	29.1%
	244	587.8	3.66E+02	4.39E+02	0.83	28.9%
	284	587.8	8.58E+02	1.12E+03	0.77	29.5%
^{98m}Nb	81	722.6	8.50E+01	7.92E+01	1.07	43.6%
		787.4	8.50E+01	5.93E+01	1.43	33.7%
	82	722.6	9.14E+01	9.07E+01	1.01	51.8%
		787.4	9.14E+01	8.81E+01	1.04	48.8%
	111	722.6	6.68E+01	8.03E+01	0.83	60.5%
		787.4	6.68E+01	8.05E+01	0.83	59.7%
	112	722.6	6.40E+01	9.48E+01	0.68	68.9%
		787.4	6.40E+01	7.35E+01	0.87	57.4%
	134	722.6	1.06E+03	5.45E+02	1.94	22.7%
		787.4	1.06E+03	5.13E+02	2.06	21.2%
	226	722.6	4.83E+01	5.48E+01	0.88	61.8%
		787.4	4.83E+01	5.26E+01	0.92	56.1%
	244	722.6	1.83E+02	1.44E+02	1.27	36.8%
		787.4	1.83E+02	1.30E+02	1.41	33.2%
	284	722.6	4.29E+02	2.97E+02	1.44	31.2%
		787.4	4.29E+02	2.82E+02	1.52	29.4%

Table B2. Calculated and experimental activities for ^{97}Nb and ^{97m}Nb peaks measured in the ASP experiments.

Nuclide	Experiment number	Peak energy (keV)	Activity (Bq)		C/E	Error (%)
			Calc.	Exp.		
^{97}Nb	81	657.9	7.97E+01	1.04E+02	0.77	25.5%
	82	657.9	8.57E+01	1.16E+02	0.74	27.9%
	111	657.9	6.26E+01	8.66E+01	0.72	30.3%
	112	657.9	5.97E+01	9.05E+01	0.66	33.6%
	134	657.9	1.16E+03	1.12E+03	1.03	17.2%
	226	657.9	4.74E+01	7.77E+01	0.61	42.0%
	244	657.9	1.90E+02	2.10E+02	0.91	24.1%
	284	657.9	4.47E+02	4.91E+02	0.91	22.9%
^{97m}Nb	81	743.4	4.90E+02	5.10E+02	0.96	38.6%
	82	743.4	5.27E+02	6.72E+02	0.78	47.6%
	111	743.4	3.85E+02	4.26E+02	0.90	43.1%
	112	743.4	3.92E+02	3.60E+02	1.09	37.5%
	226	743.4	1.47E+02	1.76E+02	0.83	54.0%
	244	743.4	2.11E+02	3.89E+02	0.54	72.2%
	284	743.4	4.96E+02	5.85E+02	0.85	51.5%

ORCID iD

M.R. Gilbert https://orcid.org/0000-0001-8935-1744

References

[1] Brooks J.N., El-Guebaly L., Hassanein A. and Sizyuk T. 2015 *Nucl. Fus.* **55** 043002
[2] Gilbert M.R., Packer L.W., Sublet J. and Forrest R.A. 2014 *Nucl. Sci. Eng.* **177** 291–306
[3] Rieth M. *et al* 2013 *J. Nucl. Mater.* **432** 482–500
[4] Ueda Y. *et al* 2017 *Nucl. Fus.* **57** 092006
[5] Taylor C.N., Yamauchi Y., Shimada M., Oya Y. and Hatano Y. 2017 *Fus. Sci. Tech.* **71** 491–5
[6] Edwards D.J., Garner F.A. and Gelles D.S. 2008 *J. Nucl. Mater.* **375** 370–81
[7] Maier H. *et al* 2009 *Phys. Scr.* **T138** 014031
[8] Kim H., Lee H.J. and Jang C. 2015 *Fus. Sci. Tech.* **68** 378–82
[9] Fabritsiev S.A., Gosudarenkova V.A., Potapova V.A., Rybin V.V., Kosachev L.S., Chakin V.P., Pokrovsky A.S. and Barabash V.R. 1992 *J. Nucl. Mater.* **191–4** 426–9
[10] Garner F.A., Greenwood L.R. and Edwards D.J. 1994 *J. Nucl. Mater.* **212-215** 426–30
[11] Gilbert M.R., Eade T., Bachmann C., Fischer U. and Taylor N.P. 2017 *Nucl. Fus.* **57** 046015
[12] Gilbert M.R., Eade T., Rey T., Vale R., Bachmann C., Fischer U. and Taylor N.P. 2019 *Nucl. Fus.* **59** 076015
[13] Someya Y. and Tobita K. 2012 *Plasma Fus. Res.* **7** 2405066
[14] Gilbert M.R. and Sublet J.-C. 2016 Handbook of activation, transmutation and radiation damage properties of the elements simulated using FISPACT-II & TENDL-2015; Magnetic Fusion Plants CCFE-R(16)36 UKAEA http://fispact.ukaea.uk
[15] Fischer U. *et al* 2017 *Fus. Eng. Des.* **123** 26–31
[16] Strategy for the management of solid low level radioactive waste from the non-nuclear industry in the United Kingdom; Part 1—Anthropogenic radionuclides, 12D/026, Department of Energy & Climate Change, UK 2012 https://www.gov.uk/government/publications/
[17] MCNP6 User Manual, Version 2.0 2017 ed Werner C.J., Alamos L. document number: LA-UR-17-29981, Rev. 0. Further details at http://mcnp.lanl.gov/
[18] Gilbert M.R., Eade T., Bachmann C., Fischer U. and Taylor N.P. 2018 *Fus. Eng. Des.* **136** 42–8
[19] Gilbert M.R. and Sublet J.-C. 2011 *Nucl. Fus.* **51** 043005
[20] Gilbert M.R., Sublet J.-C. and Dudarev S.L. 2017 *Nucl. Fus.* **57** 044002
[21] Sublet J.-C., Eastwood J.W., Morgan J.G., Gilbert M.R., Fleming M. and Arter W. 2017 *Nucl. Data Sheets* **139** 77–137
[22] Koning A., Rochman D., Sublet J., Dzysiuk N., Fleming M. and van der Marck S. 2019 *Nucl. Data Sheets* **155** 1–55 Special Issue on Nuclear Reaction Data
[23] Koning A.J., Rochman D. and Sublet J. 2019 TENDL-2019; Release Date: December 31 Available from https://tendl.web.psi.ch/tendl_2019/tendl2019.html
[24] Harman J. 2012 DEMO Operational Concept Description, report number: 2LCY7A, EUROfusion/ EFDA
[25] Stainer T., Gilbert M.R., Packer L.W., Lilley S., Gopakumar V. and Wilson C. 2020 Proc. of the conference of the Physics of Reactors (PHYSOR) https://www.physor2020.com
[26] Eade T., Colling B., Naish J., Packer L.W. and Valentine A. 2020 *Nucl. Fus.* **60** 056024
[27] The Ionising Radiations Regulations, SI 2017/1075, UK Government 2017 https://www.legislation.gov.uk/uksi/2017/1075/contents/made
[28] Work with ionising radiation, Ionising Radiations Regulations 2017, Approved Code of Practice and Guidance, L121, Health and Safety Executive (HSE), UK, 2018 https://www.hse.gov.uk/pUbns/priced/l121.pdf
[29] Gilbert M.R., Fleming M. and Sublet J.-C. 2017 *EPJ Conf.* **146** 09017
[30] Fleming M., Stainer T., and Gilbert M.R. 2018 The FISPACT-II User Manual, UKAEA-R(18)001, UKAEA, available from http://fispact.ukaea.uk
[31] Conn R.W., Okula K. and Johnson A.W. 1978 *Nucl. Tech.* **41** 389–400
[32] El-Guebaly L., Massaut V., Tobita K. and Cadwallader L. 2008 *Fus. Eng. Des.* **83** 928–35
[33] Basic principles of radioactive waste management, Revision 2, Office for Nuclear Regulation (ONR), UK 2015 www.onr.org.uk/
[34] Geological Disposal: Upstream Optioneering, Overview and uses of the 6 cubic metre concrete box, Technical Note no. 18959097, Nuclear Decommissioning Authority 2013 https://rmw.nda.gov.uk
[35] Upstream Optioneering—ILW/LLW Opportunities; Identification of potential opportunities for ILW/LLW boundary wastes introduced by changing disposal route, RWMD/04/065, AMEC for NDA, 2014 https://rmw.nda.gov.uk
[36] Lindau R. *et al* 2005 *Fus. Eng. Des.* **75–79** 989–96
[37] Smirnov A.Y., Bonarev A.K., Sulaberidze G.A., Borisevich V.D., Kulikov G.G. and Shmelev A.N. 2015 *Physics Procedia* **72** 126–31
[38] Noda T., Suzuki H., Araki H., Lyman J.L. and Newnam B.E. 2002 *J. Nucl. Mater.* **307-311** 715–18
[39] Martynenko Y.V. 2009 *Phys.-Usp.* **52** 1266–72
[40] Smith M.L. 2013 Electromagnetic enrichment of stable isotopes *Prog. Nucl. Phys.* **6** 162–6
[41] Möslang A. *et al* 2005 *Nucl. Fus.* **45** 649–55
[42] Tavassoli F. 2013 *Procedia Eng.* **55** 300–8
[43] Federici G., Biel W., Gilbert M., Kemp R., Taylor N. and Wenninger R. 2017 *Nucl. Fus.* **57** 092002
[44] Federici G. *et al* 2018 *Fus. Eng. Des.* **136** 729–41
[45] Shang Z., Ding J., Fan C., Song M., Li J., Li Q., Xue S., Hartwig K. and Zhang X. 2019 *Acta Mater.* **169** 209–24
[46] Li Y., Du J., Li L., Gao K., Pang X. and Volinsky A.A. 2020 *Eng. Fail. Anal.* **111** 104451
[47] Morgan L.W.G., Shimwell J. and Gilbert M.R. 2015 *Fus. Eng. Des.* **90** 79–87
[48] Shmelev A.N. and Kozhahmet B.K. 2017 *J. Phys.: Conf. Series* **781** 012022
[49] Hernández F. and Pereslavtsev P. 2018 *Fus. Eng. Des.* **137** 243–56
[50] Fleming M., Sublet J.-C., Gilbert M.R., Koning A. and Rochman D. 2017 *EPJ Conf.* **146** 02033
[51] Mosteller R.D. 2003 Bibliography of MCNP Verification and Validation: 1990-2003, LA-UR-03-9032, LANL, https://mcnp.lanl.gov/pdf_files/la-ur-03-9032.pdf
[52] Maekawa F. and Ikeda Y. 2000 *Fus. Eng. Des.* **47** 377–88
[53] Maekawa F., Shibata K., Wada M., Ikeda Y. and Takeuchi H. 2002 *J. Nucl. Sci. Tech.* **39** 990–3
[54] Maekawa F. and others 1998 Data collection of fusion neutronics benchmarking experiment conducted at FNS/ JAERI, JAERI-Data/Code 98-021, JAEA www.jaea.go.jp/jaeri/
[55] Maekawa F. and others 1998 Compilation of benchmark results for fusion related nuclear data, JAERI-Data/Code 98-024, JAEA www.jaea.go.jp/jaeri/
[56] Maekawa F., Wada M., and Ikeda Y. 1999 Decay Heat Experiment and Validation of calculation code systems for fusion reactor, JAERI 99-055, JAEA www.jaea.go.jp/jaeri/

[57] Gilbert M.R. and Sublet J. 2019 *Nucl. Fus.* **59** 086045
[58] Gilbert M.R., Vilkhivskaya O. and Sublet J.-C. 2020 Fusion decay heat validation, FISPACT-II & TENDL-2019, ENDF/B-VIII.0, JEFF-3.3, EAF2010 and IRDFF-II nuclear data libraries, UKAEA-CCFE-RE(20)04, UKAEA available from http://fispact.ukaea.uk
[59] Gilbert M.R., Packer L.W. and Lilley S. 2014 *Nucl. Data Sheets* **119** 401–3
[60] Packer L.W., Angelone M., Gilbert M.R., Loreti S., Nobs C.R., Pillon M., Sublet J.-C. and Vilkhivskaya O. 2020 Proc. of the conference of the Physics of Reactors (PHYSOR) https://www.physor2020.com
[61] Packer L.W., Gilbert M.R., Hughes S., Lilley S., Pampin R. and Sublet J.-C. 2012 *Fus. Eng. Des.* **87** 662–6
[62] Packer L.W., Hughes S., Gilbert M.R., Lilley S. and Pampin R. 2013 *Fus. Eng. Design.* **88** 2617–20
[63] Lilley S., Packer L.W., Pampin R. and Gilbert M.R. 2013 *Fus. Eng. Des.* **88** 2629–30
[64] Packer L.W., Gilbert M.R. and Lilley S. 2014 *Nucl. Data Sheets* **119** 173–5
[65] Forrest R.A. 2006 *Fus. Eng. Des.* **81** 2143–56
[66] Forrest R.A. 2011 *Ene. Procedia* **7** 540–52
[67] Currie L.A. 1968 *Analytical Chem.* **40** 586–93
[68] Kirkpatrick J.M. and Young B.M. 2009 *IEEE Trans. Nucl. Sci.* **56** 1278–82
[69] Pommé S., Fitzgerald R. and Keightley J. 2015 *Metrologia* **52** S3–S17
[70] Krane K.S. 1988 *Introductory Nuclear Physics* (New York, US: Wiley)
[71] EXFOR: Experimental Nuclear Reaction Data www-nds.iaea.org/exfor/
[72] Koning A.J. and Rochman D. 2018 TENDL-2017; Release Date: April 25 Available from https://tendl.web.psi.ch/tendl_2017/tendl2017.html
[73] Boulby Underground Germanium Suite (BUGS) - Ultra-low Background Assay; Boulby Underground Laboratory, UK Science & Technology Facilities Council (STFC) https://www.boulby.stfc.ac.uk/Pages/Ultra-low%20Background%20Material%20Screening.aspx
[74] Davies A.V., Burnett J.L. and Britton R. 2020 *Nucl. Instrum. Methods Phys. Res., Sect.* A **951** 163009
[75] Britton R., Jackson M.J. and Davies A.V. 2015 *J. Environ. Radioact.* **149** 158–63
[76] Becker J.S. 2003 *Spectrochim. Acta, Part* B **58** 1757–84
[77] Clases D., Birka M., Sperling M., Faust A. and Karst U. 2017 *J.Trace Elem. Med. Biol.* **40** 97–103
[78] Ibarra A. *et al* 2018 *Nucl. Fus.* **58** 105002